



# Enhanced efficiency of MoS<sub>2</sub>/SnO<sub>2</sub> nanocomposite as a catalyst for the photodegradation of methylene blue

Asad Naseem<sup>1</sup>, Yasir A. Haleem<sup>1,a)</sup> , Sheheera Irfan<sup>1</sup>, Muhammad Usman<sup>1,a)</sup>, Naseeb Ahmad<sup>5</sup>, Muhammad Arshad<sup>2</sup>, Muhammad Imran Irshad<sup>1</sup>, Muhammad Farooq Saleem<sup>3</sup>, Rashid Khan<sup>4</sup>

<sup>1</sup> Institute of Physics, Khwaja Fareed University of Engineering and Information Technology, Rahim Yar Khan 64200, Pakistan

<sup>2</sup> Nano Sciences and Technology Department, National Centre for Physics, Quaid-E-Azam University Campus, Islamabad 45320, Pakistan

<sup>3</sup> GBA Branch of Aerospace Information Research Institute, Chinese Academy of Sciences, Guangzhou 510700, China

<sup>4</sup> Zhejiang Provincial Key Laboratory of Advanced Chemical Engineering Manufacture Technology, College of Chemical and Biological Engineering, Zhejiang University, Hangzhou 310027, China

<sup>5</sup> Department of Physics, Baba Guru Nanak University, Nankana Sahib 39100, Pakistan

<sup>a)</sup> Address all correspondence to these authors. e-mails: hiyasir@mail.ustc.edu.cn; yasir.haleem@kfueit.edu.pk; dr.usman@kfueit.edu.pk; zakrian2003@gmail.com

Received: 27 February 2024; accepted: 19 August 2024

In this work, the characteristics of MoS<sub>2</sub> and its nanocomposite with SnO<sub>2</sub> for photocatalytic degradation of methylene blue have been investigated. The MoS<sub>2</sub> and MoS<sub>2</sub>/SnO<sub>2</sub> nanocomposites were synthesized by the hydrothermal method. SEM analysis shows the flower-like structure of MoS<sub>2</sub> while MoS<sub>2</sub>/SnO<sub>2</sub> nanocomposites shows grain-like structure. The EDX analysis of the MoS<sub>2</sub> and MoS<sub>2</sub>/SnO<sub>2</sub> nanocomposites confirm the samples were mainly composed of Mo, S, Sn, and O atoms and the XRD patterns confirm hexagonal and rhombohedral phases, respectively. The FTIR spectra indicate the presence of both hydroxyl and carboxyl functional groups at the sample's surface. The UV-Visible spectroscopy findings witness both samples are being active in the visible range. Further, the band gap estimation through Tauc plot supports the assertion that these materials could be an efficient catalyst for photodegradation. Furthermore, the photodegradation of methylene blue (used as a dye) findings declare the maximum efficiency of 93% by using MoS<sub>2</sub>/SnO<sub>2</sub> nanocomposite as a catalyst.

## Introduction

With the rapid expansion of urbanization and industry, the disposal of industrial effluent including diverse organic and inorganic contaminants such as synthetic colors, antibiotics, and toxic substances has created major contamination. Among these contaminants, organic dyes are significant environmental pollutants, which are used in various manufacturing areas such as the cosmetic industry, leather products, paper, and fabrics [1, 2]. Several dyes stay in sewage for a long time, posing serious harm to the environment due to their quick rate of disintegration in aqueous solutions and remarkable resistance to light, heat, and chemicals. Around 10,000 distinct varieties of dyes and pigments, an average of 735 tons, are produced globally [3–6]. Anionic, cationic, and non-ionic dyes are the three main categories of dyes. The greatest class of organic dyes is thought to be anionic dyes, which are those that contain nitrogen-nitrogen double bonds [7]. Methylene blue (MB), a common anionic dye

that is water soluble, is typically released into the environment along with wastewater from businesses that produce textiles, drugs, food, and paper. Because they constitute a major danger to the chemical and physical characteristics of water and aquatic life, these contaminants must be eliminated using the necessary techniques [8]. Organic synthetic colors and dyes present in many industrial wastes substantially damage the environment since they cannot be broken down by standard treatment procedures due to their complex aromatic structure and high stability against temperature, water, chemicals, and light. This viewpoint has made the breakdown of organic color molecules in wastewater a top priority [9, 10]. There are numerous techniques that have been utilized to remove dyes such as precipitation [11], photocatalysis (PC) [12], adsorption [13], anaerobic and aerobic treatments [14, 15].

The photocatalytic degradation of industrial dyes has recently been a key area where transition metal oxides and transition metal dichalcogenides have been playing a crucial role

[16]. Air, water, soil, and land contamination are just a few of the many ways that environmental pollution can appear. The general threat of pollution is exacerbated by the discharge of hazardous materials into the environment, including toxic metals, gaseous pollutants, particulate matter, and a host of human activities like sewage, industrial effluents, agricultural runoff, and disposing of electronic waste [17]. A revolutionary and environmentally friendly PC method transforms solar energy to catalyst molecules which could contribute to the degradation of MB [18]. Hazardous contaminants can be eliminated with PC methods, but undesirable byproducts may still remain. This strategy is affordable, orderly, and easy to control [19]. Due to their potential use in air and water purification, semiconducting photocatalysts have attracted a lot of attention [20]. Under feasible circumstances a semiconductor photocatalyst with appropriate bandgap energy may absorb photons of solar energy and create two positive holes ( $h^+$ ) and negative electrons ( $e^-$ ). Following photoexcitation, the surface of the semiconductors receives these photoinduced charge carriers, which start redox reactions [21].

In the fields of energy storage, energy conversion, and photocatalytic applications, a number of transition metal dichalcogenides, including ( $MoS_2$ ,  $CuS$ ,  $SnS$ ,  $WS_2$ , and  $ZnS$ ), have been extensively employed [22, 23]. Molybdenum disulfide ( $MoS_2$ ) is a 2-D substance with an S–Mo–S layered structure connected by covalent connections. Further, low-cost techniques like hydrothermal and chemical vapor deposition may readily and quickly synthesize  $MoS_2$  in large amounts [1, 24]. It serves as a battery material, sensor, adsorbent, catalyst, and more [25]. Recently,  $MoS_2$ -based composites have been exploited for photocatalytic degradation of industrial dyes. But there has been a lot of research work need to be done to fully understand the environmental remediation of this photocatalytic degradation of industrial dyes. Yet, it is critical to thoroughly examine the process and mechanism of degradation using  $MoS_2$  based nanocomposites. The high rate of photo-generated electron–hole pair recombination, weak electrical conductivity, and low energy density of pure  $MoS_2$  restrict its use in photocatalytic applications. However,  $MoS_2$  does exhibit improved photocatalytic efficacy when combined with other semiconducting metal oxides, though. A variety of metal oxides, including  $RuO_2$ ,  $MnO_2$ ,  $SnO_2$ ,  $CoO$ ,  $NiO$ ,  $Fe_2O_3$ , have been employed successfully for photocatalytic applications. Tin oxide ( $SnO_2$ ) stands out among them due to its favorable properties, which include being inexpensive, non-toxic, chemically stable, having a high charge transfer, and having a significant electrochemical activity.  $SnO_2$  might potentially be used as a photocatalyst material because of its good characteristics. One of the best of these is molybdenum disulfide ( $MoS_2$ ), which has a layered crystal structure akin to that of graphene and is more readily available and less expensive than the others.

Due to its greater stability compared to 1T- $MoS_2$  and 3R- $MoS_2$ , 2H- $MoS_2$  is the most widely utilized polytype of  $MoS_2$ . There have been reports of 2H- $MoS_2$  in several different morphologies, including nanorods [26], nanotubes [27], nanoflowers, inorganic fullerenes [28], and spherical particles [29].  $MoS_2$  has been produced using a variety of techniques, including hydrothermal synthesis, chemical vapor desorption, and electrochemical and chemical approaches [30]. The kind of  $MoS_2$  structure that results is dependent on the synthesis technique utilized. For instance, it is well known that the hydrothermal process, when used under moderate operating conditions, may provide well-crystallized  $MoS_2$  with a straightforward approach [31]. Additionally, other  $MoS_2$  particle morphologies, such as spherical, nanotube, and nanoflower particles, may be produced hydrothermally [32]. In order to selectively regenerate fine molecules and reduce aromatic compounds under solar light, current research has involved synthesizing and constructing a photoreactor setup as a photocatalyst [33, 34].

In the current study, we examined the characteristics of  $MoS_2/SnO_2$  nanocomposites made by simple hydrothermal method and utilized it for photocatalytic degradation of MB. Morphological, compositional, functional group, phase purity, crystal structure, and optical properties were all examined using Scanning Electron Microscopy (SEM), Energy Dispersive X-ray spectra (EDS), Fourier Transform Infrared Spectroscopy (FTIR), X-ray Powder Diffraction (XRD), and Ultraviolet–Visible spectroscopy (UV–VIS) techniques, respectively. For the  $MoS_2/SnO_2$  nanocomposites, the photodegradation efficiency was seen to be enhanced, and pertinent experimental findings are thoroughly presented. Further, the computational calculations were performed to support the efficient charge transfer mechanism from the photocatalyst surface during photodegradation processes. Furthermore, the synergy among the experimental findings and the computational calculations presents the good understanding of the mechanism responsible for the excellent photocatalytic degradation of methylene blue. This study could be valuable for advancing photocatalytic degradation technologies and their potential applications for real-world societal needs.

## Results and Discussion

The remarkable physical, chemical, and mechanical characteristics of  $MoS_2$  make it a top contender for next-generation semiconducting materials. It is crucial to synthesize highly crystalline  $MoS_2$  in order to use it as a promising layered material for potential applications. We have adopted hydrothermal method for the synthesis of our samples as given in the materials and methods section. We have particularly synthesized four samples, i.e., one is pure  $MoS_2$ , and three nanocomposites containing  $MoS_2$  with varying weight percent of  $SnO_2$ . The samples were named as P1 for pure  $MoS_2$ , C1 for  $MoS_2/SnO_2$  (with 20%), C2

for MoS<sub>2</sub>/SnO<sub>2</sub> (with 40%), and C3 for MoS<sub>2</sub>/SnO<sub>2</sub> (with 60%), respectively. Further, we characterized our samples using different techniques. Scanning Electron Microscopy (SEM) is used to identify the morphology of synthesized samples.

In Fig. 1(a) SEM micrograph shows the Flower-like structure of pure MoS<sub>2</sub> (P1) but when we prepare MoS<sub>2</sub>/SnO<sub>2</sub> nanocomposites it converts into grains as shown in Fig. 1(b). The transformation from flower-like structure to grains is due to different reaction kinematics for the preparation of MoS<sub>2</sub>/SnO<sub>2</sub> (C2) nanocomposites [35]. The Energy Dispersive X-ray Spectroscopy (EDX) confirmed P1 is mainly composed of atoms of Mo and S in excess amounts.

The prominent EDX peaks for Mo and S have been observed at 2.29 and 2.30 keV energy, respectively, as shown in the Fig. 1(c). There are two different peaks at 2.29 and 2.81 keV energies for Mo atoms representing the transitions from K and

L shells, respectively. The peak for O atoms at 0.5 keV energy might come from the oxygen-based surface functional groups.

The Fig. 1(d) represents EDX spectroscopy for the nanocomposites of MoS<sub>2</sub>/SnO<sub>2</sub>. There are noticeable peaks observed for Mo, S, Sn, and O atoms at 2.29, 2.30, 3.4, and 0.5 keV energies, respectively, as shown in Fig. 1(d). There are different peaks at (3.1 KeV, 3.5 KeV, 3.9 KeV and 4.3 KeV) energies for Sn atoms representing the transitions from K, L, and M-shells, respectively. The EDX spectra for nanocomposite contain pronounced peak for oxygen atoms indicating the presence of SnO<sub>2</sub> with MoS<sub>2</sub>. The notable C atoms peaks present in both (P1 & C2) EDX spectra might come from carbon-based substrate utilized for EDX testing.

For the identification of the functional group at the surface of P1 and C2 samples, we used Fourier Transformed Infrared Spectroscopy (FTIR). The FTIR spectra of P1, C1, C2, and C3

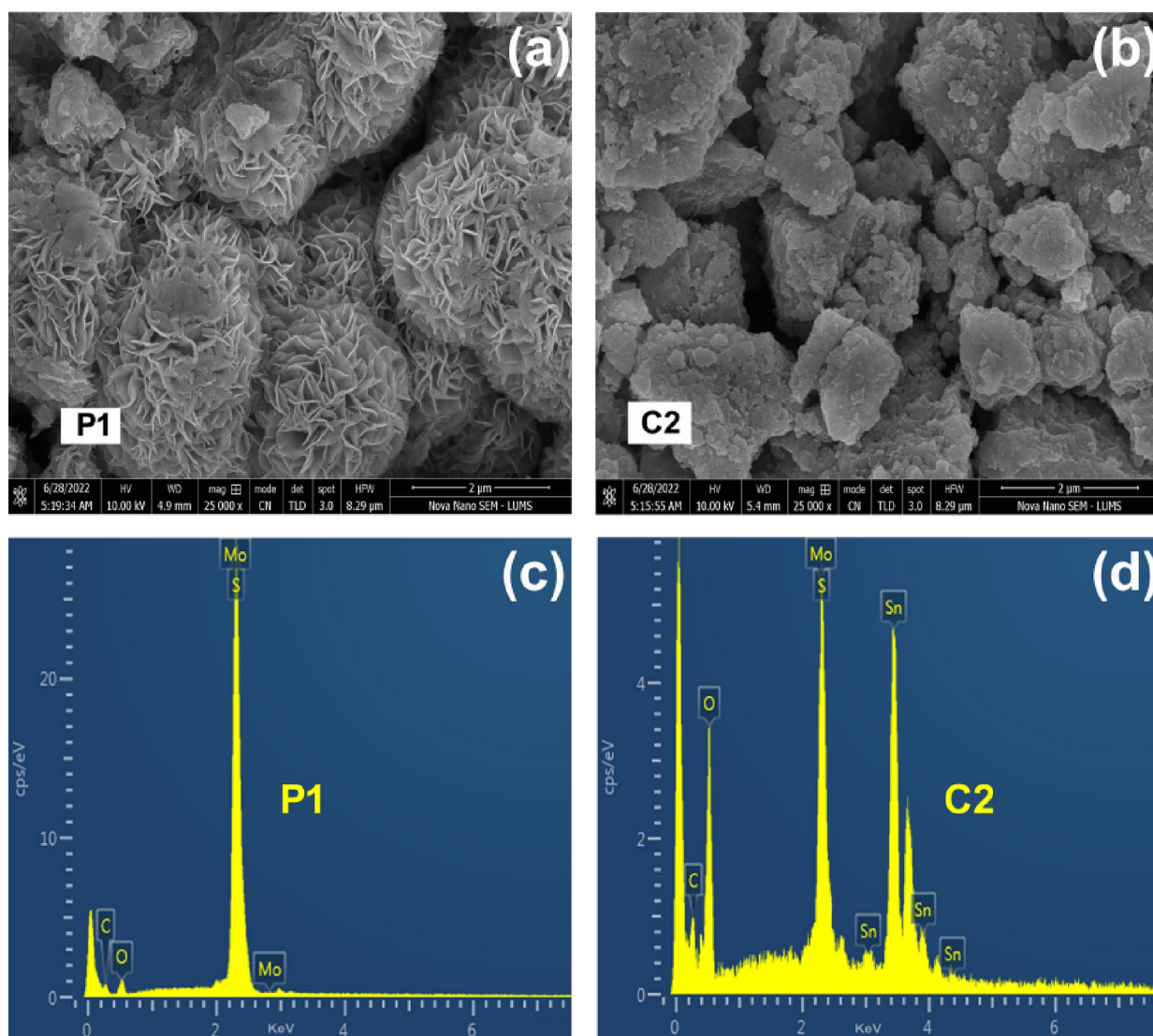


**Figure 1:** SEM micrographs of (a) pure MoS<sub>2</sub>, (b) MoS<sub>2</sub>/SnO<sub>2</sub> nanocomposites, EDX spectra of (c) pure MoS<sub>2</sub> and (d) MoS<sub>2</sub>/SnO<sub>2</sub> nanocomposites.

samples are shown in the Fig. 2. The FTIR spectra confirm the presence of hydroxyl and carboxyl functional groups at the surface of the samples. The appearances of different stretching and bending peaks are discussed briefly. Here, we have the FTIR pattern of P1 ( $\text{MoS}_2$  nanoparticles) as shown in Fig. 2(a). The peaks at  $1991\text{cm}^{-1}$  represented the C-H bending vibrations. The peak at  $2367\text{cm}^{-1}$  shows the stretching mode of O-H bonds [36]. The two distinct peaks are shown at  $1397$  and  $1502\text{cm}^{-1}$ . The peak at  $1397\text{cm}^{-1}$  corresponded to the C=O [37]. The peak at  $1502\text{cm}^{-1}$  represented the C-O [38]. The FTIR pattern for the  $\text{MoS}_2$  material indicates the presence of both hydroxyl and carboxyl groups.

The FTIR Spectra of C1, C2, and C3 ( $\text{MoS}_2/\text{SnO}_2$  nanocomposites) are shown in Fig. 2(b). The peak at  $2367\text{cm}^{-1}$  shows the stretching mode of O-H bonds [36]. The broad peak at  $1134\text{cm}^{-1}$  was appeared because of the OH molecules absorption causing the hydroxyl to stretch and vibrate [39]. The peak at  $3210\text{cm}^{-1}$  was due to the H-O-H stretching vibration [40]. The peaks at  $1991\text{cm}^{-1}$  represented the C-H bending vibration. The peaks at  $1397\text{cm}^{-1}$  corresponded to the C=O [37] and the peak at  $1502\text{cm}^{-1}$  represented the C-O vibrations [38]. The FTIR pattern for the  $\text{MoS}_2/\text{SnO}_2$  nanocomposites indicates the presence of both hydroxyl and carboxyl groups.

The X-Ray Diffraction (XRD) was utilized to investigate the crystalline nature of selected samples P1 and C2 as shown in Fig. 3. The powder X-ray diffraction (XRD) pattern demonstrated that the P1 (pure  $\text{MoS}_2$ ) is crystalline and peaks matched with the JCPDS card no. 17-0744 as shown in the Fig. 3(a). The XRD pattern reveals that the peaks were centered at  $2\theta$  (hkl) values of  $14.45^\circ$  (003),  $29.34^\circ$  (006),  $33.11^\circ$  (101),  $41.10^\circ$  (015), and  $52.12^\circ$  (018), respectively. These diffraction peaks indicate the presence of hexagonal and rhombohedral phases [24, 41].

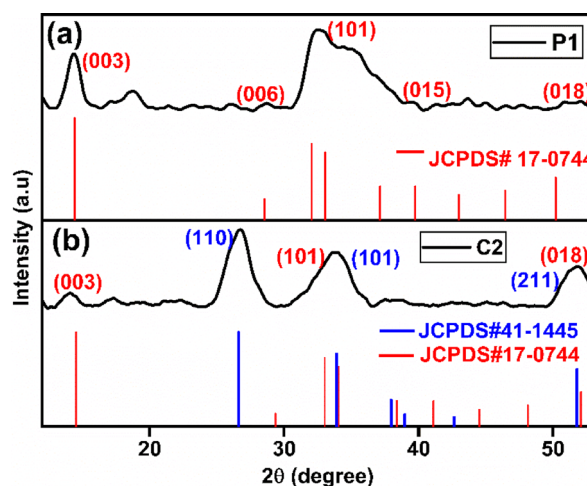


Figure 3: XRD patterns of (a) pure  $\text{MoS}_2$  and (b)  $\text{MoS}_2/\text{SnO}_2$  nanocomposites.

Figure 3(b), the XRD data for sample C2, also display diffraction peaks linked to  $\text{SnO}_2$ , along with peaks for  $\text{MoS}_2$  according to JCPDS card nos. 41-1445 and 17-0744, respectively. The presence of  $\text{SnO}_2$  diffraction peaks in  $\text{MoS}_2/\text{SnO}_2$  nanocomposite samples, demonstrates that  $\text{SnO}_2$  had been incorporated successfully. The XRD pattern reveals that the peaks were centered at  $2\theta$  (hkl) values of  $14.45^\circ$  (003),  $26.63^\circ$  (110),  $33.86^\circ$  (101),  $51.78^\circ$  (211), and  $52.12^\circ$  (018) (JCPDS card no. 41-1445) [42, 43].

Further, Ultraviolet Visible (UV-Vis) spectroscopy was used to probe the optical properties of samples P1, C1, C2, and C3. The samples were examined in the  $400\text{--}800\text{nm}$  wavelength range in order to mark their photoactivity as shown in Fig. 4. It has been observed that all the samples are active in

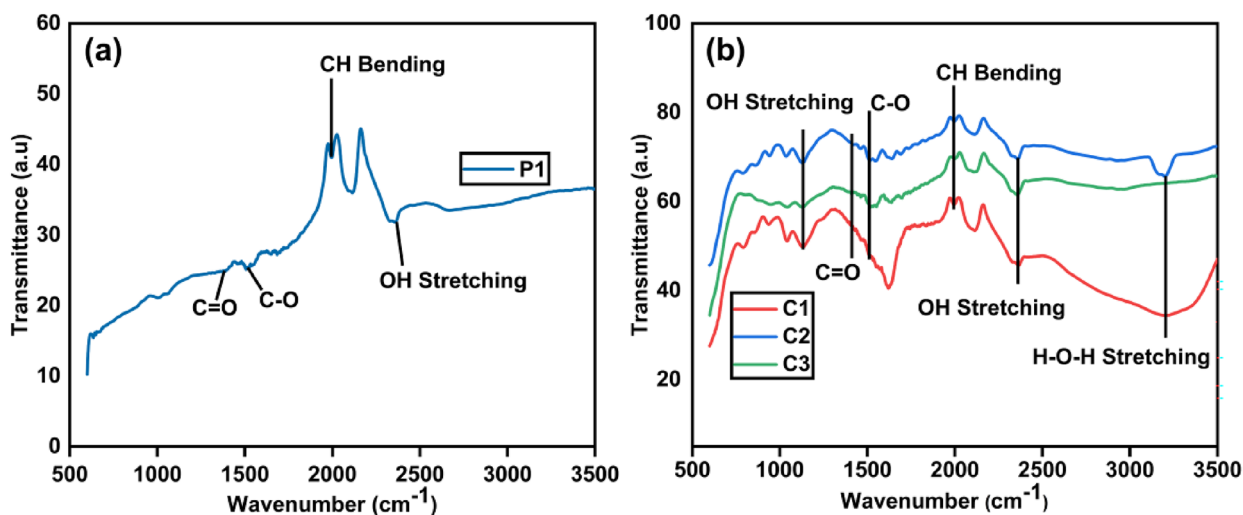
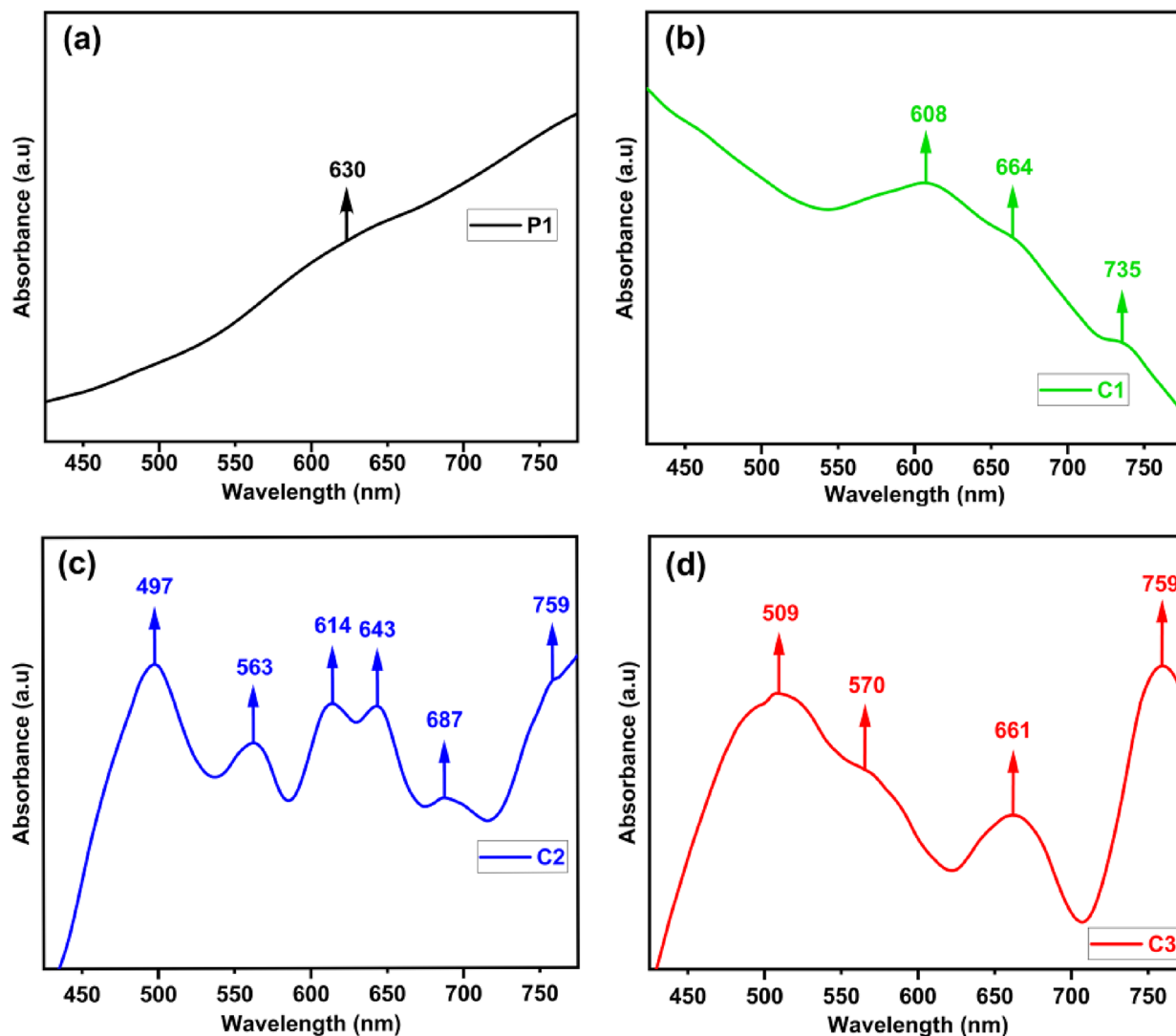


Figure 2: FTIR spectra of (a) pure  $\text{MoS}_2$  and (b)  $\text{MoS}_2/\text{SnO}_2$  nanocomposites.



**Figure 4:** UV-Visible spectra of (a) pure MoS<sub>2</sub> named as P1 and (b–d) MoS<sub>2</sub>/SnO<sub>2</sub> nanocomposites with different SnO<sub>2</sub> concentrations named as C1, C2, and C3 respectively.

the visible range. No prominent absorption peak was observed in the UV-Vis spectrum of sample P1 instead an imperceptible hump appeared about 630 nm as shown in Fig. 4(a). It was also observed that the intensity of absorption increases with the increase of wavelength within the visible range for sample P1. The addition of SnO<sub>2</sub> enhanced the photoactivity of the nanocomposites. In sample C1 minor bulges were observed about 608nm, 664nm, and 735nm. For sample C2 various peaks were observed at 487, 563, 614, 643, 687, and 759 nm, respectively. The presence of these peaks indicates the higher photoactivity of sample C2 within 400–800 nm wavelength range. In sample C3, again multiple peaks observed at 509nm, 570nm, 661nm, and 759nm. But for C3 at higher wavelengths the absorption intensities decrease about 600–700 wavelength range which was not observed for C2. On the basis of UV-Vis spectra analysis

we could infer that the sample C2 could demonstrate high performance as a photocatalyst in comparison with P1, C1, and C3 samples. No prominent absorption peak was observed in the UV-Vis spectrum of pure SnO<sub>2</sub> as shown in the Fig. S1.

Moreover, the estimation of the band gap energy for each sample was done by using the Tauc plot. The Tauc plots for samples P1, C1, C2, and C3 are shown in the Fig. 5. The estimated band gap of P1 is 1.8 eV as shown in Fig. 5(a). This indicates that the photoactivity of P1 is higher close to the borderline of visible region with infrared region. The addition of SnO<sub>2</sub> has increased the band gap for C1, C2, and C3. The estimated band gaps for C1, C2, and C3 are 2.16, 2.34, and 2.47 eV, respectively, as shown in Fig. 5(b)–(d) [44]. The increase in band gap energies for C1, C2, and C3 infers higher photoactivity in the low wavelength range from 400 to 600 nm. This contemplates that

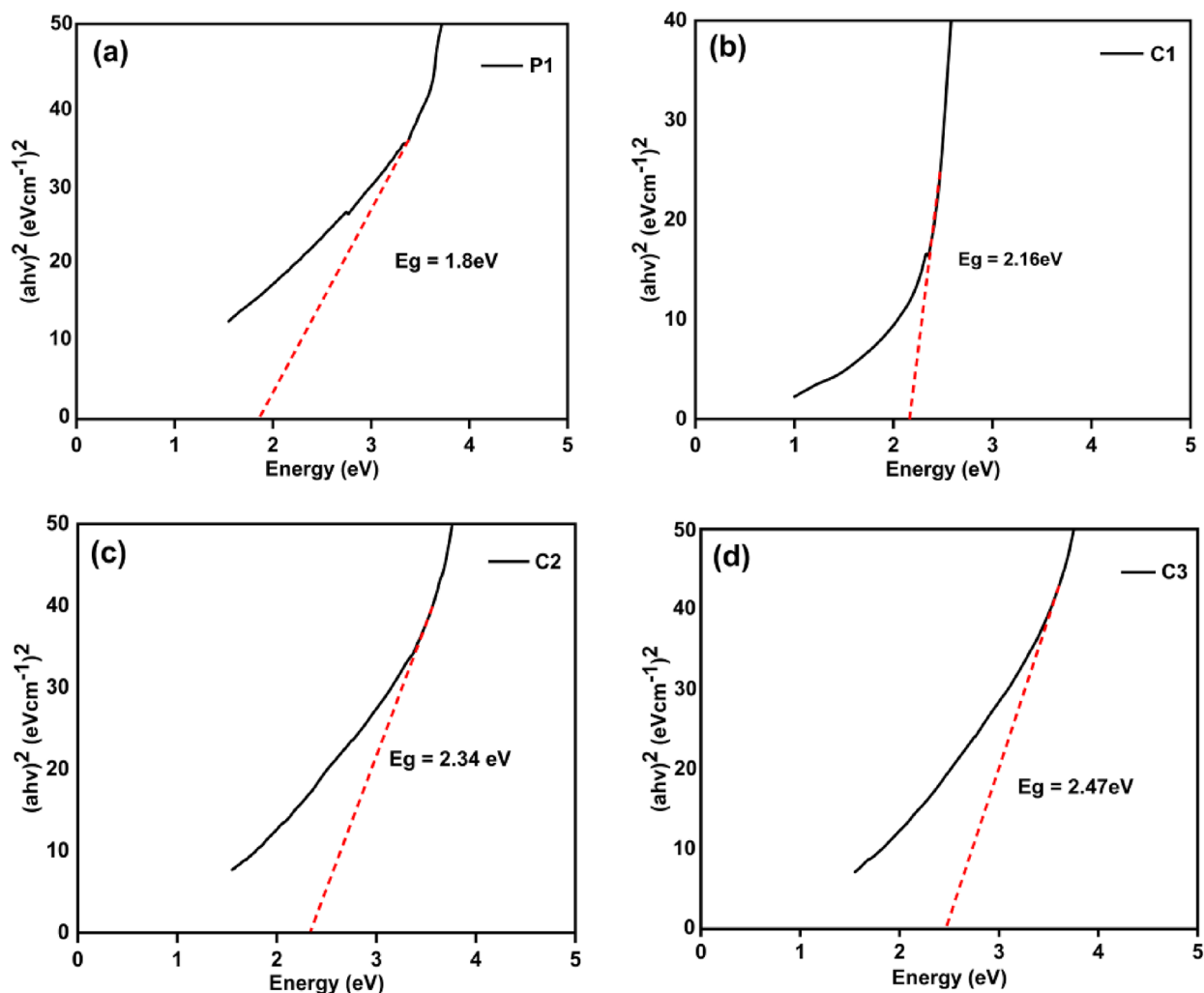


**Figure 5:** Estimation of band gap using Tauc plot of (a) pure MoS<sub>2</sub> named as P1 and (b–d) MoS<sub>2</sub>/SnO<sub>2</sub> nanocomposites with different SnO<sub>2</sub> concentrations named as C1, C2, and C3 respectively.

the nanocomposites samples C1, C2, and C3 could achieve high photoactivity as compare with P1 sample. Furthermore, in order to take advantage of anticipated high photoactivity of nanocomposites as a photocatalyst, an experiment involving the photo-degradation of Methylene Blue (MB) was carried out at room temperature.

The Fig. 6 elucidates the UV–Vis spectra of samples (P1, C1, C2, and C3) as photocatalyst at specific time intervals, i.e., 0, 50, 100, 150, and 200 min during photodegradation of MB under UV irradiations. A typical UV–Vis absorption peak for MB solution ranges from 550 to 700 nm as shown in Fig. 6. It was observed that the MB absorption peak intensity was reduced as the time passed from 0 to 200 min. The smaller peak intensity for P1 as the time of 200 min passed indicates the incomplete photodegradation of MB as shown in Fig. 6(a). Similarly, for sample C1 a minor bulge was observed as an absorption peak after time of 200 min as indicated by Fig. 6(b). However, this

absorption peak was entirely disappeared at time 200 min indicates the complete photodegradation of MB for sample C2 as illustrated by Fig. 6(c). A small hump as an absorption peak at time 200 min for sample C3 validates the presence of small amount of MB as shown in Fig. 6(d). Subsequently, the percentage photodegradation efficiency of all the samples (P1, C1, C2, and C3) at specific time intervals is illustrated as a bar graph in the Fig. 7(a). The P1 sample shows MB photodegradation of 59, 69, 73, and 78% at 0, 50, 100, 150, and 200 min, respectively. The C1 sample demonstrates MB photodegradation of 69, 74, 79, and 83% at 0, 50, 100, 150, and 200 min, respectively. Similarly, the C2 sample demonstrates MB photodegradation of 80, 85, 89, and 93% at 0, 50, 100, 150, and 200 min, respectively. Lastly, the C3 sample demonstrates MB photodegradation of 73, 77, 82, and 87% at 0, 50, 100, 150, and 200 min, respectively. Clearly, we can infer that C2 sample has shown better photodegradation performance as compared to all other samples (P1, C1, and C3).

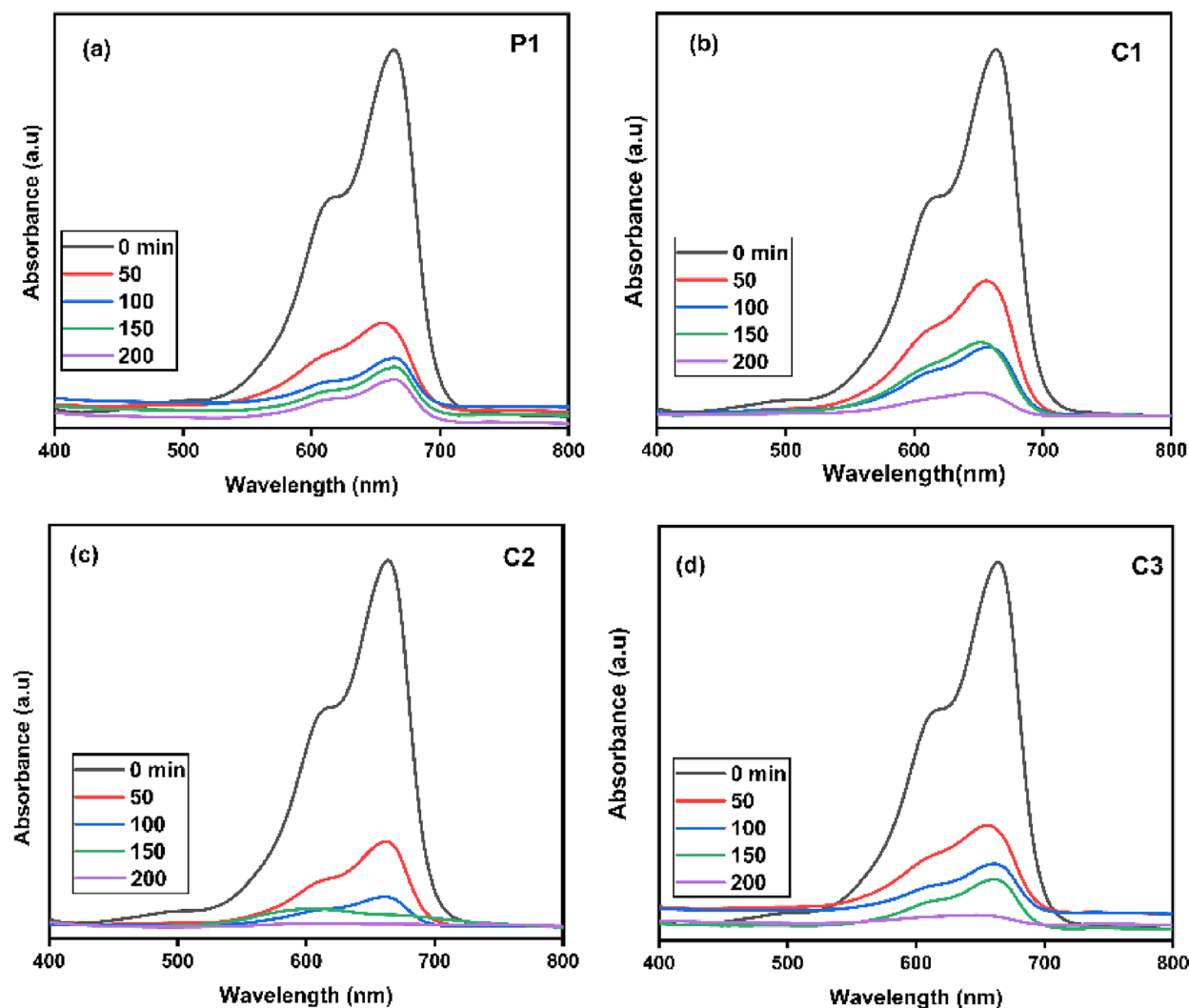


**Figure 6:** UV-Visible spectra of Methylene Blue taken at different time intervals during photocatalytic degradation under UV irradiation using (a) pure MoS<sub>2</sub> named as P1 and (b–d) MoS<sub>2</sub>/SnO<sub>2</sub> nanocomposites with different SnO<sub>2</sub> concentrations named as C1, C2 and C3 respectively as photocatalyst.

Therefore, we can assuredly deduce that C2 is more efficient than others. This might be explained by the increased surface area of, which may offer more active sites on the surface for reactant molecules and boost the effectiveness of the electron–hole separation [45]. We have also performed the photodegradation of MB by using pure SnO<sub>2</sub> as a photocatalyst, but no degradation activity was observed as shown in the Fig. S2. Additionally, the surface imperfections such as oxygen vacancies and crystalline defects play a key role in improving photocatalytic efficiency. Ultimately, we could ascertain that the optimal amount of SnO<sub>2</sub> for nanocomposite (MoS<sub>2</sub>/SnO<sub>2</sub>) for efficient photodegradation of MB is about 40%. Besides, the Fig. 7(b), (c) illustrates the kinetic studies of photocatalytic mechanism for photodegradation of MB.

MoS<sub>2</sub>/SnO<sub>2</sub> nanocomposites may now be used practically because of SnO<sub>2</sub>'s dual role in improving photocatalytic

performance and increasing the photostability of the MoS<sub>2</sub> material. Further, we used the equation given below to estimate the photodegradation reaction kinetics. The pseudo-first-order reaction and the apparent first-order reaction rate constant (*k*) derived from the formula are obeyed by the photocatalytic process.

$$-\ln\left(\frac{C}{C_0}\right) = kt$$

where *C*<sub>0</sub> is the dye's starting concentration and *C* represents the dye's concentration at different points in time *t* and *k* represents rate constant for kinetic studies of photocatalytic degradation [46].

The kinetic parameters were calculated assuming that the degradation rate follows a pseudo-first-order kinetics as shown in the Fig. 7(b), (c). The rate constant (*k*) for the

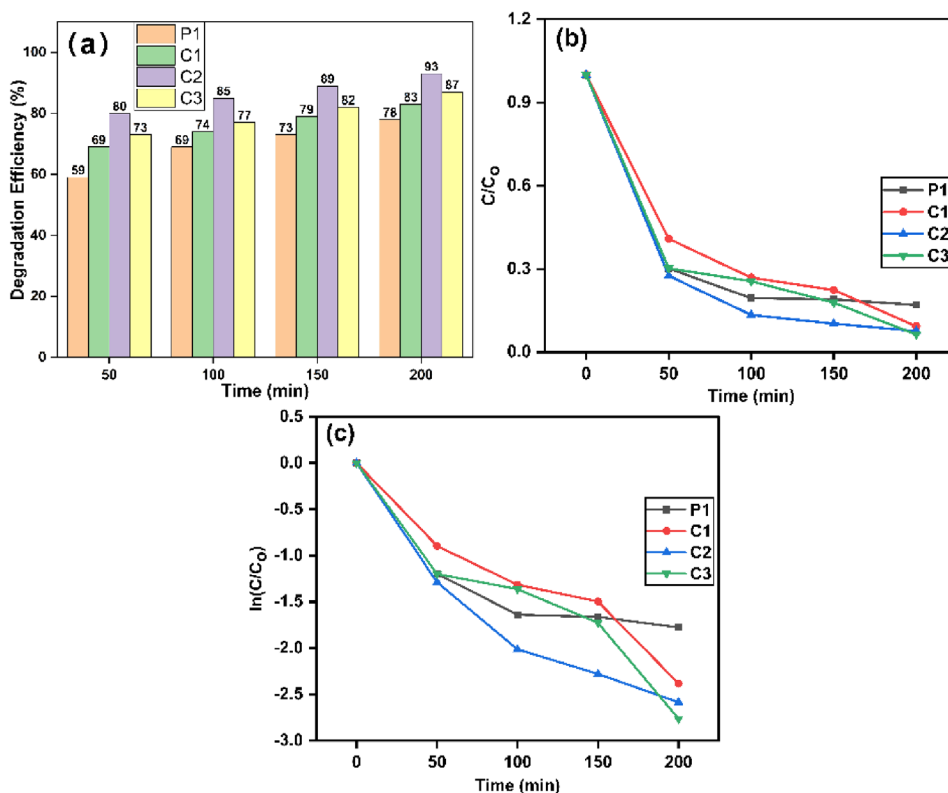


**Figure 7:** Comparison of (a) degradation efficiency (%), and (b, c) Kinetics of MB photodegradation under UV irradiation for pure MoS<sub>2</sub> named as P1 and MoS<sub>2</sub>/SnO<sub>2</sub> nanocomposites with different SnO<sub>2</sub> concentrations named as C1, C2 and C3 respectively.

**Table 1:** Estimated rate constants (k) for the degradation of MB under UV irradiations for pure MoS<sub>2</sub> named as P1 and MoS<sub>2</sub>/SnO<sub>2</sub> nanocomposites with different SnO<sub>2</sub> concentrations named as C1, C2 and C3 respectively.

Sample no	Samples name	Rate (min <sup>-1</sup> )
1	P1	1.257 × 10 <sup>-2</sup>
2	C1	1.389 × 10 <sup>-2</sup>
2	C2	1.85 × 10 <sup>-2</sup>
4	C3	1.6 × 10 <sup>-2</sup>

degradation of MB by P1, C1, C2, and C3 were estimated to be 1.257 × 10<sup>-2</sup> min<sup>-1</sup>, 1.389 × 10<sup>-2</sup> min<sup>-1</sup>, 1.85 × 10<sup>-2</sup> min<sup>-1</sup>, and 1.61 × 10<sup>-2</sup> min<sup>-1</sup>, respectively as given in Table 1. This shows that among all the synthesized samples, MoS<sub>2</sub>/SnO<sub>2</sub> exhibited the most pronounced photocatalytic performance. The efficient transfer of photo-induced electrons from the conduction band of MoS<sub>2</sub> to the SnO<sub>2</sub> prevents the chances of recombination between the excited electrons and holes, which is responsible for the enhanced photocatalytic performance of the MoS<sub>2</sub>/SnO<sub>2</sub>. However, the photocatalytic activity of MoS<sub>2</sub>/SnO<sub>2</sub> composites at higher % of SnO<sub>2</sub> was found to be decreased, even though they possess stronger visible light absorption and a higher adsorption of dyes.

In the case of nanocomposites, it may have been possible that the addition of SnO<sub>2</sub> may lead to formation of an appropriate band structure that is well suited for the separation of electron-hole pair at the interface between the nanocomposite and MB solution as shown in the Fig. 8(a). This could be resulted as an effective transfer of the electrons from the VB to CB, leaving the holes behind. The MoS<sub>2</sub>/SnO<sub>2</sub> nanocomposites are therefore better able to photocatalyze the breakdown of MB dye as a result [47]. The electron-hole pairs' recombination, however, caused the samples to exhibit poor photodegradation. The edge locations of the conduction and valence bands of the two materials will unite to form a single structure, as illustrated in Fig. 8 and as a result, both charge carriers are transported to the MoS<sub>2</sub> interface. The electrons in SnO<sub>2</sub> and MoS<sub>2</sub>'s VB are excited to the CB band, leaving a hole on the VB, when the photon energy is greater than or equal to the band gap energy of those materials. Rapid recombination leaves just a small number of charge carriers available for the photocatalytic activity. However, because SnO<sub>2</sub> has a more negative CB potential than MoS<sub>2</sub>, the electrons that are liberated after exciting it with light from the CB of SnO<sub>2</sub> are transferred to the CB of MoS<sub>2</sub> at the MoS<sub>2</sub>/SnO<sub>2</sub> interface, leading to an effective separation of electron-hole pairs under the influence of light. Therefore, SnO<sub>2</sub> in the composite plays a crucial role in increasing photostability and photocatalytic activity of MoS<sub>2</sub> [48]. In the subsequent stage, free



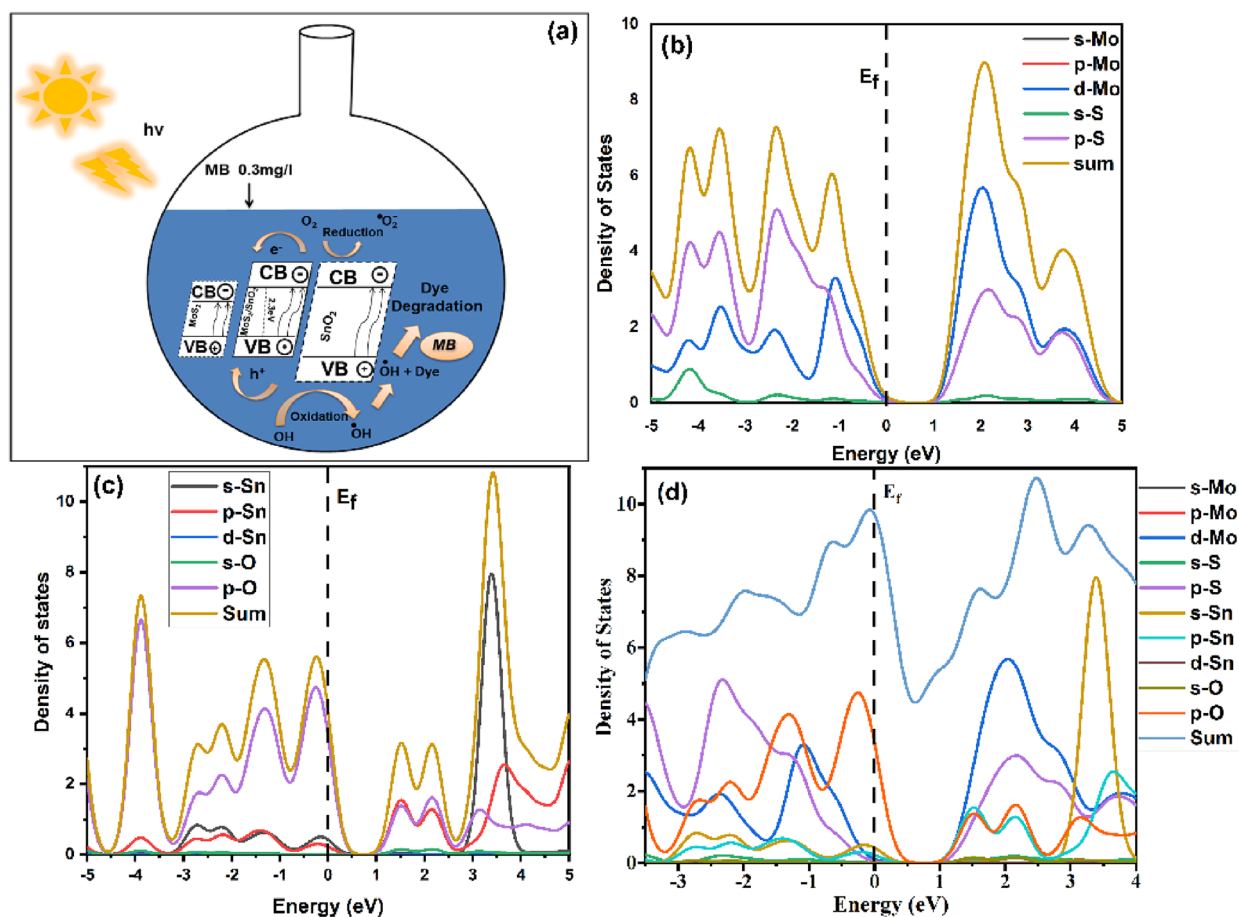
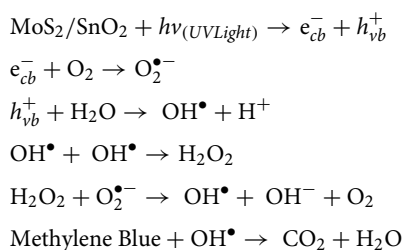


**Figure 8:** (a) Schematic diagram of the mechanism of photocatalytic degradation of MB under UV irradiation and DFT based calculations of density of states using CASTEP module of (b) MoS<sub>2</sub>, (c) SnO<sub>2</sub> and (d) MoS<sub>2</sub>/SnO<sub>2</sub> nanocomposite.

electrons in the conduction bands (CB) of both MoS<sub>2</sub> and SnO<sub>2</sub> interact with ambient O<sub>2</sub> to produce oxygen radicals (O<sub>2</sub><sup>•-</sup>). In the next phase, water molecules create a hydroxyl radical by saturating the photocatalyst's hole. O<sub>2</sub><sup>•-</sup> and H<sup>+</sup> are involved in the breakdown of the MB aqueous solution because of their strong reactivity. In the last stage, the dye combines with hydroxyl radicals to produce CO<sub>2</sub> gas and H<sub>2</sub>O, which dramatically reduces the amount of dye. The equations representing the stepwise process for MB photodegradation according to Kapatel et al. [51] are given below.



According to literature [49–52], the breakdown of the MB results in CO<sub>2</sub>, H<sub>2</sub>O, and a few intermediate compounds. By creating

the right conditions, the high concentration of O<sub>2</sub><sup>•-</sup> and OH<sup>•</sup> radicals in the solution controls this reaction. [53]. Therefore, it is simple to comprehend that the deeper valence band (VB) edge of MoS<sub>2</sub> and the increased photocatalytic activity of the MoS<sub>2</sub>/SnO<sub>2</sub> nanocomposites are caused by better hole transfer. It is also true that as compared to pure MoS<sub>2</sub> and SnO<sub>2</sub> or other semiconductors, MoS<sub>2</sub>/SnO<sub>2</sub> nanocomposites have a superior photodegradation rate for the MB dye. Because MoS<sub>2</sub> functions as a photosensitizer molecule in the heterojunction, SnO<sub>2</sub> may exploit the visible area after sensitization. Therefore, it is evident that the addition of MoS<sub>2</sub> to SnO<sub>2</sub> nanoparticles enhances the photocatalytic activity of the MoS<sub>2</sub>/SnO<sub>2</sub> photocatalyst for MB degradation. Other effects include reduced photogenerated charge recombination, rapid electron transfers across the heterojunction due to increased absorption toward the visible range.

Further, we conducted Density Functional Theory (DFT) calculations using the CASTEP module to estimate the partial density of states (PDOS) and analyze the orbital electronic properties of MoS<sub>2</sub>, SnO<sub>2</sub>, and their nanocomposite MoS<sub>2</sub>/SnO<sub>2</sub>. The PDOS results, presented in Fig. 8(b)–(d), indicate that MoS<sub>2</sub>

exhibits the lowest charge mobility across the Fermi level, while SnO<sub>2</sub> shows higher charge mobility compared to MoS<sub>2</sub>. Remarkably, the charge mobility significantly improves in the MoS<sub>2</sub>/SnO<sub>2</sub> nanocomposite. This enhanced charge mobility correlates with the observed high photocatalytic efficiency of the MoS<sub>2</sub>/SnO<sub>2</sub> nanocomposite. The increased density of states near the Fermi level, which facilitates efficient charge mobility, is attributed to the contributions from the p orbital of O in the MoS<sub>2</sub>/SnO<sub>2</sub> nanocomposite. Consequently, the photocatalytic performance of the MoS<sub>2</sub>/SnO<sub>2</sub> nanocomposite surpasses that of the individual photocatalytic activity of MoS<sub>2</sub> and SnO<sub>2</sub>.

## Conclusion

In this work, MoS<sub>2</sub>/SnO<sub>2</sub> nanocomposites are successfully prepared by hydrothermal method. It was observed that the pure MoS<sub>2</sub> shows a flower-like structure, whereas the nanocomposites have grain-like structure due to different reaction kinematics. The Energy Dispersive X-ray Spectroscopy confirmed the prepared samples are mainly composed of atoms of Mo, S, Sn, and O in excess amounts. The presences of the carboxyl and hydroxyl functional groups were validated with the help of FTIR spectroscopy. Moreover, UV–Visible Spectra confirmed the prepared samples demonstrate the high absorption of visible light within the wavelength range of 450–800nm. The band gap of MoS<sub>2</sub>/SnO<sub>2</sub> varies from 1.8 to 2.47 eV with varying SnO<sub>2</sub> concentrations as estimated by Tauc plots. We have employed MoS<sub>2</sub>/SnO<sub>2</sub> nanocomposites for the degradation of MB. It has been observed that photodegradation of MB using MoS<sub>2</sub>/SnO<sub>2</sub> nanocomposites is dependent on the loading amount of catalyst and time duration for photodegradation reaction. We infer from this study, that the addition of SnO<sub>2</sub> with pure MoS<sub>2</sub> make the nanocomposite highly photoactive and the optimal amount of SnO<sub>2</sub> loading for maximum efficiency was 40 wt%. About 93% MB was degraded when we used MoS<sub>2</sub>/SnO<sub>2</sub>-40 wt% nanocomposite (C2). The synergistic effect of enhanced light absorption, low electron–hole recombination due to appropriate band gap and high surface area are responsible for superior photocatalytic performance.

## Materials and methods

### Preparation of MoS<sub>2</sub>

In this work, we prepared MoS<sub>2</sub> nanostructure via hydrothermal method. Hydrothermal method is usually carried out in a pressurized vessel, known as an Autoclave. We used 1 mol of ammonium molybdate and 5 mol of thiourea solutions separately prepared in distilled water. In the next step, the 100 mL Teflon beaker was filled with the solutions prepared in the previous step upto 70% by volume. The filled Teflon beaker was

put inside the autoclave and kept in the oven for 24 h at 180 °C. After completion of the 24 h the autoclave was removed from the oven and let it dry at ambient conditions. Later, the Teflon beaker was removed from the autoclave and the inside solution containing the reaction products were transferred to 50 mL plastic tubes for washing. The ethanol and deionized water were used to wash the reaction products via precipitation by using centrifugation machine. The washing cycles were repeated several times. After washing, the obtained precipitated slurry was dried in the oven overnight at 80 °C. Finally, MoS<sub>2</sub> was obtained as a black powder. The schematic of synthesis is given in the Fig. 9.

Further, the liquid exfoliation process is used to make MoS<sub>2</sub> nanostructures. In a 50 mL solution of Ethanol and DI water, 0.15 g of MoS<sub>2</sub> powder is disseminated (1:1 volume ratio). At room temperature, the solution is ultra-sonicated continuously for 12 h. The dispersion color changes from grayish-black to greenish after 12 h of sonication, indicating that the exfoliation was successful. To remove the greater remaining MoS<sub>2</sub>, the dispersion was centrifuged at 4000 rpm for 6 min. The supernatant was removed carefully and the residue powder was collected as pure MoS<sub>2</sub> (named P1).

### Preparation of nano-composites

For the preparation of MoS<sub>2</sub>/SnO<sub>2</sub> nanocomposites, we used tin dichloride SnCl<sub>2</sub>·2H<sub>2</sub>O as tin precursor and pure MoS<sub>2</sub> prepared in the last step, 0.1gm of SnCl<sub>2</sub>·2H<sub>2</sub>O was added to 50 mL of exfoliated pure MoS<sub>2</sub> and sonicated for 24 h. After that, the solution was refluxed for 2 h at 80 °C, and finally, sample (C1) is ready. Similarly, repeat the above procedure for samples (C2) and (C3) using concentrations of 0.5 and 1 g, respectively. Lastly, all prepared samples P1, C1, C2, and C3 were characterized using SEM, EDX, XRD, and UV–Vis spectroscopy. The photocatalytic activity of all the samples (P1, C1, C2, and C3) was tested by the degradation of MB.

### Computational investigation

For the computational investigations of material, we use the DFT based simulation code, i.e., CASTEP to utilize the pseudo potentials for the density of states and electronic band structure. We use the Perdew–Burke–Ernzerhof (PBE) for generalized gradient approximation (GGA) in our estimations. For this purpose, P63/MMC space group was used with the symmetry of 3 × 3 × 1 supercell. The plane wave cut off energy is 381 eV. The maximum Hellmann–Feynman force is 0.05 eV/Å, the ionic displacement is 0.02 Å and maximum stress is 0.1 GPa.



**Figure 9:** Schematic diagram of hydrothermal method for the synthesis of MoS<sub>2</sub>.

### Setup for photocatalytic activity

MB solution degradation under visible light illumination was used to assess the photocatalytic activity of P1, C1, C2, and C3 samples. The dye solution was prepared by adding a certain concentration (for example, 200 mL,  $C_0 = 10 \text{ mg L}^{-1}$ ) of MB and a specific amount of samples (P1, C1, C2, and C3) were poured into the MB solution for photodegradation. Once the solution had reached an equilibrium state throughout, for more than 30 min, as it was stirred ferociously with a magnetic stirrer in a dark environment. A UV-Vis spectrophotometer operating at a wavelength of 664 nm was used to determine the concentration of the aqueous suspensions (MB) in each sample. A 125 W high-pressure mercury lamp was used as a visible light source. The samples and MB solution were exposed to UV radiation with 25 cm spacing between the UV lamp and the glass beaker containing MB dye solution. The photocatalytic efficiency was estimated using the formula  $= (1 - C/C_0)$ , where  $C_0$  is the MB concentration before illumination and  $C$  is the MB concentration after a specific amount of exposure time.

### Acknowledgments

Funding for this work was provided by Project No. 20-12058 from the Higher Education Commission (HEC) of Pakistan under the supports of the National Research Program for Universities (NRPU).

### Author contributions

Asad Naseem: Methodology; Data curation; Formal analysis; Writing—original draft. Yasir A. Haleem: Conceptualization; Supervision; Visualization; Investigation; Validation; Writing—revision & editing. Sheheera Irfan: Formal analysis; Software; Data curation; Writing—original draft. Muhammad Usman: Supervision; Funding acquisition; Resources; Writing—revision & editing. Naseeb Ahmad: Formal analysis; Resources; Writing—revision & editing. Muhammad Arshad: Formal analysis; Resources; Characterizations; Writing—revision & editing. Muhammad Imran Irshad: Formal analysis; Writing—revision & editing. Muhammad Farooq Saleem: Formal analysis; Writing—revision & editing. Rashid Khan: Formal analysis; Writing—revision & editing.

### Funding

Funding for this work was provided by Project No. 20-12058 from the Higher Education Commission (HEC) of Pakistan under the supports of the National Research Program for Universities (NRPU).

### Data availability

Data will be made available on reasonable request.

### Declarations

**Conflict of interest** The authors declare no conflict of interest.

## Supplementary Information

The online version contains supplementary material available at <https://doi.org/10.1557/s43578-024-01426-1>.

## References

- S. Han, K. Liu, L. Hu, F. Teng, P. Yu, Y. Zhu, Superior adsorption and regenerable dye adsorbent based on flower-like molybdenum disulfide nanostructure. *Sci. Rep.* **7**(1), 43599 (2017)
- M. Barreto-Rodrigues, J. Silveira, J.A. Zazo, J.J. Rodriguez, Rodriguez: Synthesis, characterization and application of nanoscale zero-valent iron in the degradation of the azo dye Disperse Red. *J. Environ. Chem. Eng.* **15**(1), 628 (2017)
- S. Singh, N. Verma, A. Umar, S.K. Kansal, ZnCdS nanoparticles decorated three-dimensional MoO<sub>3</sub> polygonal structure: A novel photocatalyst for enhanced solar light-driven degradation of methyl orange dye. *J. Alloys Compd.* **997**, 174714 (2024)
- V.K. Gupta, R. Jain, A. Nayak, S. Agarwal, M. Shrivastava, Removal of the hazardous dye—Tartrazine by photodegradation on titanium dioxide surface. *Mater. Sci. Eng. C* **31**(5), 1062 (2011)
- M.V. Subbaiah, D.S. Kim, Adsorption of methyl orange from aqueous solution by aminated pumpkin seed powder: kinetics, isotherms, and thermodynamic studies. *Ecotoxicol. Environ. Saf.* **128**, 109 (2016)
- B. Ulas, M. Ergun, Biosorption of remazol orange RR from aqueous solution: kinetic, equilibrium and thermodynamic studies. *Desal. Water Treatm.* **163**, 366 (2019)
- L. Zheng, C. Wang, Y. Shu, X. Yan, L. Li, Utilization of diatomite/chitosan–Fe (III) composite for the removal of anionic azo dyes from wastewater: equilibrium, kinetics and thermodynamics. *Colloids Surf A Physicochem Eng Asp* **468**, 129 (2015)
- W. Cheah, S. Hosseini, M.A. Khan, T.G. Chuah, T.S. Choong, Acid modified carbon coated monolith for methyl orange adsorption. *Chem. Eng. J.* **215**, 747 (2013)
- B.K. Ghosh, S. Hazra, B. Naik, N.N. Ghosh, Preparation of Cu nanoparticle loaded SBA-15 and their excellent catalytic activity in reduction of variety of dyes. *Powder Technol.* **269**, 371 (2015)
- P. Saikia, A.T. Miah, P.P. Das, Highly efficient catalytic reductive degradation of various organic dyes by Au/CeO<sub>2</sub>-TiO<sub>2</sub> nano-hybrid. *J. Chem. Sci.* **129**, 81 (2017)
- M.X. Zhu, L. Lee, H.H. Wang, Z. Wang, Removal of an anionic dye by adsorption/precipitation processes using alkaline white mud. *J. Hazard. Mater.* **149**(3), 735 (2007)
- X.Z. Li, K.L. Wu, C. Dong, S.H. Xia, Y. Ye, X.W. Wei, Size-controlled synthesis of Ag<sub>3</sub>PO<sub>4</sub> nanorods and their high-performance photocatalysis for dye degradation under visible-light irradiation. *Mater. Lett.* **130**, 97 (2014)
- X. Sun, Y. Zhou, X. Zheng, Comparison of adsorption behaviors of Fe-La oxides co-loaded MgO nanosheets for the removal of methyl orange and phosphate in single and binary systems. *J. Environ. Chem. Eng.* **8**(5), 104252 (2020)
- C. O'Neill, A. Lopez, S. Esteves, F.R. Hawkes, D.L. Hawkes, S. Wilcox, Azo-dye degradation in an anaerobic-aerobic treatment system operating on simulated textile effluent. *Applied Microbiol. Biotechnol.* **53**, 249 (2000)
- A. Vijeata, G.R. Chaudhary, S. Chaudhary, A. Umar, Biogenic synthesis of highly fluorescent carbon dots using *Azadirachta indica* leaves: an eco-friendly approach with enhanced photocatalytic degradation efficiency towards Malachite green. *Chemosphere* **341**, 139946 (2023)
- V.A. Tran, T.K. Phung, T.K. Vo, T.T. Nguyen, T.A. Nguyen, D.Q. Viet, V.Q. Hieu, T.T. Vo, Solar-light-driven photocatalytic degradation of methyl orange dye over Co<sub>3</sub>O<sub>4</sub>-ZnO nanoparticles. *Mater. Lett.* **284**, 128902 (2021)
- M. Sharma, S. Sharma, M.S. Akhtar, R. Kumar, A. Umar, A.A. Alkhanjaf, S. Baskoutas, Microorganisms-assisted degradation of Acid Orange 7 dye: a review. *Int. J. Environ. Sci. Technol.* **21**(7), 6133 (2024)
- R. Singh, R.K. Yadav, S. Singh, R. Shahin, A. Umar, A.A. Ibrahim, O. Singh, N.K. Gupta, C. Singh, J.O. Baeg, S. Baskoutas, Nature-inspired polymer photocatalysts for green NADH regeneration and nitroarene transformation. *Chemosphere* **353**, 141491 (2024)
- M. Kaur, S. Singh, S.K. Mehta, S.K. Kansal, A. Umar, A.A. Ibrahim, S. Baskoutas, CeO<sub>2</sub> quantum dots decorated g-C<sub>3</sub>N<sub>4</sub> nanosheets: a potential scaffold for fluorescence sensing of heavy metals and visible-light driven photocatalyst. *J. Alloys Compd.* **960**, 170637 (2023)
- S.A. Ansari, N. Parveen. Enhanced photocatalytic degradation of organic pollutants using iron lanthanum oxide nanoparticles *MatSci Express* **1**(1), 28–32 (2024). <https://doi.org/10.69626/mse.2024.0028>
- S.A. Ansari, N. Parveen, G.M. Alsulaim, A.A. Ansari, S.A. Alsharif, K.M. Alnahdi, H.A. Alali, V.R. Reddy, Emerging NiO-rGO nanohybrids for antibiotic pollutant degradation under visible-light irradiation. *Surfaces Interfaces* **40**, 103078 (2023)
- C.N. Rao, K. Gopalakrishnan, U. Maitra, Comparative study of potential applications of graphene, MoS<sub>2</sub>, and other two-dimensional materials in energy devices, sensors, and related areas. *ACS Appl. Mater. Interfaces* **7**(15), 7809 (2015)
- K. Gopalakrishnan, S. Sultan, A. Govindaraj, C.N. Rao, Supercapacitors based on composites of PANI with nanosheets of nitrogen-doped RGO, BC1. 5N, MoS<sub>2</sub> and WS. *Nano Energy* **212**, 52 (2015)
- K. Chang, W. Chen, L-cysteine-assisted synthesis of layered MoS<sub>2</sub>/graphene composites with excellent electrochemical performances for lithium ion batteries. *ACS Nano* **5**(6), 4720 (2011)
- J. Chen, Y. Liao, X. Wan, S. Tie, B. Zhang, S. Lan, X. Gao, A high performance MoO<sub>3</sub>@ MoS<sub>2</sub> porous nanorods for adsorption and photodegradation of dye. *J. Solid State Chem.* **291**, 121652 (2020)

26. C. Zhang, H.B. Wu, Z. Guo, X.W. Lou, Facile synthesis of carbon-coated MoS<sub>2</sub> nanorods with enhanced lithium storage properties. *Electrochem. Commun.* **20**, 7 (2012)
27. M. Remskar, A. Mrzel, M. Virsek, M. Godec, M. Krause, A. Kolitsch, A. Singh, A. Seabaugh, The MoS<sub>2</sub> nanotubes with defect-controlled electric properties. *Nanoscale Res. Lett.* **6**, 1 (2011)
28. I. Wiesel, R. Popovitz-Biro, R. Tenne, Encapsulation of Mo<sub>2</sub>C in MoS<sub>2</sub> inorganic fullerene-like nanoparticles and nanotubes. *Nanoscale* **5**(4), 1499 (2013)
29. M.A. Ramos, V. Correa, B. Torres, S. Flores, J.R. Farias Mancilla, R.R. Chianelli, Spherical MoS<sub>2</sub> micro particles and their surface dispersion due to addition of cobalt promoters. *Rev. Mexicana Física* **57**(3), 220 (2011)
30. Q. Li, J.T. Newberg, E.C. Walter, J.C. Hemminger, R.M. Penner, Polycrystalline molybdenum disulfide (2H-MoS<sub>2</sub>) nano- and microribbons by electrochemical/chemical synthesis. *Nano Lett.* **4**(2), 277 (2004)
31. R. Wei, H. Yang, K. Du, W. Fu, Y. Tian, Q. Yu, S. Liu, M. Li, G. Zou, A facile method to prepare MoS<sub>2</sub> with nanoflower-like morphology. *Mater. Chem. Phys.* **108**(2–3), 188 (2008)
32. L. Ma, W.X. Chen, H. Li, Y.F. Zheng, Z.D. Xu, Ionic liquid-assisted hydrothermal synthesis of MoS<sub>2</sub> microspheres. *Mater. Lett.* **62**(6–7), 797 (2008)
33. V. Gupta, R.K. Yadav, A. Umar, A.A. Ibrahim, S. Singh, R. Shahin, R.K. Shukla, D. Tiwary, D.K. Dwivedi, A.K. Singh, A.K. Singh, Highly efficient self-assembled activated carbon cloth-templated photocatalyst for NADH regeneration and photocatalytic reduction of 4-nitro benzyl alcohol. *Catalysts* **13**(4), 666 (2023)
34. S.A. Ansari, Elemental semiconductor red phosphorus/ZnO nanohybrids as high performance photocatalysts. *Ceram. Int.* **49**(11), 17746 (2023)
35. S. Asaithambi, P. Sakthivel, M. Karuppaiah, K. Balamurugan, R. Yuvakkumar, M. Thambidurai, G. Ravi, Synthesis and characterization of various transition metals doped SnO<sub>2</sub>@ MoS<sub>2</sub> composites for supercapacitor and photocatalytic applications. *J. Alloys Comps.* **853**, 157060 (2021)
36. I. Zahariev, M. Piskin, E. Karaduman, D. Ivanova, I. Markova, L. Fachikov. FTIR spectroscopy method for investigation of Co–Ni nanoparticle nanosurface phenomena. *J. Chem. Technol. Metall.* **52**(5) (2017). <https://openurl.ebsco.com/EPDB%3Agcd%3A2%3A4879698/detailv2?sid=ebsco%3Aplink%3Ascholar&id=ebsco%3Agcd%3A124138612&crl=c>
37. X. Feng, Q. Tang, J. Zhou, J. Fang, P. Ding, L. Sun, L. Shi, Novel mixed-solvothermal synthesis of MoS<sub>2</sub> nanosheets with controllable morphologies. *Cryst. Res. Technol.* **48**(6), 363 (2013)
38. R. Lamba, A. Umar, S.K. Mehta, S.K. Kansal, Sb<sub>2</sub>O<sub>3</sub>–ZnO nanospindles: a potential material for photocatalytic and sensing applications. *Ceram. Int.* **41**(4), 5429 (2015)
39. P. Ghasemipour, M. Fattahi, B. Rasekh, F. Yazdian, Developing the ternary ZnO doped MoS<sub>2</sub> nanostructures grafted on CNT and reduced graphene oxide (RGO) for photocatalytic degradation of aniline. *Sci. Rep.* **10**(1), 4414 (2020)
40. R. Lamba, A. Umar, S.K. Mehta, S.K. Kansal, CeO<sub>2</sub>ZnO hexagonal nanodisks: Efficient material for the degradation of direct blue 15 dye and its simulated dye bath effluent under solar light. *J. Alloys Comps.* **620**, 67 (2015)
41. H. Lin, X. Chen, H. Li, M. Yang, Y. Qi, Hydrothermal synthesis and characterization of MoS<sub>2</sub> nanorods. *Mater. Lett.* **64**(15), 1748 (2010)
42. P. Xing, P. Chen, Z. Chen, X. Hu, H. Lin, Y. Wu, L. Zhao, Y. He, Novel ternary MoS<sub>2</sub>/C–ZnO composite with efficient performance in photocatalytic NH<sub>3</sub> synthesis under simulated sunlight. *ACS Sustain. Chem. Eng.* **6**(11), 14866 (2018)
43. S. Asaithambi, P. Sakthivel, M. Karuppaiah, G.U. Sankar, K. Balamurugan, R. Yuvakkumar, M. Thambidurai, G. Ravi, Investigation of electrochemical properties of various transition metals doped SnO<sub>2</sub> spherical nanostructures for supercapacitor applications. *J. Energy Storage* **31**, 101530 (2020)
44. R. Ameta, M.S. Solanki, S. Benjamin, S.C. Ameta. Photocatalysis In: *Advanced oxidation processes for waste water treatment* (Elsevier, 2018), pp. 135. <https://doi.org/10.1016/B978-0-12-810499-6.00006-1>. <https://www.sciencedirect.com/science/article/abs/pii/B9780128104996000061>
45. Y. Wang, L. Zhang, K. Deng, X. Chen, Z. Zou, Low temperature synthesis and photocatalytic activity of rutile TiO<sub>2</sub> nanorod superstructures. *J. Phys. Chem. C* **111**(6), 2709 (2007). <https://doi.org/10.1021/jp066519k>
46. S. Vadivel, G. Rajarajan, Influence of Cu doping on structural, optical and photocatalytic activity of SnO<sub>2</sub> nanostructure thin films. *J. Mater. Sci. Mater. Electron.* **26**, 5863 (2015)
47. C.V. Ramana, U. Becker, V. Shutthanandan, C.M. Julien, Oxidation and metal-insertion in molybdenite surfaces: evaluation of charge-transfer mechanisms and dynamics. *Geochem. Trans.* **9**, 1 (2008)
48. Y. Min, G. He, Q. Xu, Y. Chen, Dual-functional MoS<sub>2</sub> sheet-modified CdS branch-like heterostructures with enhanced photostability and photocatalytic activity. *J. Mater. Chem. A* **2**(8), 2578 (2014)
49. Y. Ahmed, Z. Yaakob, P. Akhtar, Degradation and mineralization of methylene blue using a heterogeneous photo-Fenton catalyst under visible and solar light irradiation. *Catal. Sci. Technol.* **6**(4), 1222 (2016)
50. J. Luan, Z. Hu, Synthesis, property characterization, and photocatalytic activity of novel visible light-responsive photocatalyst. *Int. J. Photoenergy* **2012**, 1 (2012)
51. S. Kapatel, C.K. Sumesh, Two-step facile preparation of MoS<sub>2</sub> · ZnO nanocomposite as efficient photocatalyst for methylene blue (dye) degradation. *Electron. Mater. Lett.* **15**, 119 (2019)

52. F. Liu, J. Zhao, Y. Ma, Z. Liu, Y. Xu, H. Zhang, Removal of diesel from soil washing effluent by electro-enhanced Fe<sup>2+</sup> activated persulfate process. *J. Electroanal. Chem.* **906**, 115995 (2022)
53. A. Ajmal, I. Majeed, R.N. Malik, H. Idriss, M.A. Nadeem, Principles and mechanisms of photocatalytic dye degradation on TiO<sub>2</sub> based photocatalysts: a comparative overview. *Rsc Adv* **4**(70), 37003 (2014)

**Publisher's Note** Springer Nature remains neutral with regard to jurisdictional claims in published maps and institutional affiliations.

Springer Nature or its licensor (e.g. a society or other partner) holds exclusive rights to this article under a publishing agreement with the author(s) or other rightsholder(s); author self-archiving of the accepted manuscript version of this article is solely governed by the terms of such publishing agreement and applicable law.